



Pergamon

Acta Materialia 50 (2002) 2737–2745



www.actamat-journals.com

Processing, microstructure and properties of ductile metal particulate reinforced $\text{Zr}_{57}\text{Nb}_5\text{Al}_{10}\text{Cu}_{15.4}\text{Ni}_{12.6}$ bulk metallic glass composites

H. Choi-Yim^{a,*}, R.D. Conner^b, F. Szuecs^a, W.L. Johnson^a

^a W.M. Keck Laboratory of Engineering Materials, Mail Code 138-78, California Institute of Technology, Pasadena, CA 91125, USA

^b Luxfer, Inc., 3016 Kansas Ave., Riverside, CA 92507, USA

Received 5 October 2001; received in revised form 25 February 2002; accepted 25 February 2002

Abstract

The $\text{Zr}_{57}\text{Nb}_5\text{Al}_{10}\text{Cu}_{15.4}\text{Ni}_{12.6}$ bulk metallic glass forming liquid is reinforced with up to 50 Volume-percent (% V_f) Ta, Nb, or Mo particles. An extensive reaction layer of varying composition formed in the metallic–glass matrix surrounding the particles. A characterization based on X-ray diffraction, differential scanning calorimeter, electron microprobe, and scanning electron microscopy is presented. The composites were tested in compression and tension. Compressive strain-to-failure increased by up to a factor of 12 compared to the unreinforced $\text{Zr}_{57}\text{Nb}_5\text{Al}_{10}\text{Cu}_{15.4}\text{Ni}_{12.6}$ bulk metallic glass. The increase in compressive strain-to-failure is due to the particles restricting shear band propagation, promoting the generation of multiple shear bands and additional fracture surface area. © 2002 Acta Materialia Inc. Published by Elsevier Science Ltd. All rights reserved.

Keywords: Metallic glass; Composites; Mechanical properties; Fracture

1. Introduction

Because of its high strength and high elastic strain limit, metallic glass is a natural candidate for use as reinforcement in composite materials. There have been a number of attempts to produce composites with amorphous ribbon reinforcements [1–3]; these attempts usually incorporate the melt spinning technique [4,5]. Amorphous metallic alloys have also been used as a matrix for particu-

late and fiber-reinforced composites [6,7]. The development of bulk metallic–glass forming alloys has opened new opportunities for fabrication of composites incorporating a bulk metallic–glass matrix. These include the Zr–Ti–Ni–Cu–Be [8], Zr–Ti–Cu–Ni [9], and Zr–Ti(Nb)–Cu–Ni–Al [10] alloys with critical cooling rates for glass formation in the range from 1 to 100 Ks^{-1} . The Zr–Nb–Cu–Ni–Al alloy is known to be one of the best glass formers, and fully amorphous rods of up to 1 cm in diameter have been cast with this alloy. This alloy is very robust against heterogeneous nucleation at surfaces or interfaces, making it desirable for use as the matrix in the development of novel bulk metallic

* Corresponding author.

E-mail address: hchoi@its.caltech.edu (H. Choi-Yim).

glass-matrix composites [11,12]. The Zr-Nb-Cu-Ni-Al alloy was reinforced with tantalum (Ta), niobium (Nb), and molybdenum (Mo) particles. These particles have limited reactivity, good wettability and thermal-expansion coefficients (α) and Poisson ratios (ν) similar to that of the matrix. The physical properties of the matrix and reinforcement are listed in Table 1.

Zr-Nb-Cu-Ni-Al alloy has high yield strength (1.8 GPa), high elastic strain limit (2%), moderate stiffness (86 GPa), and a tendency to fail catastrophically along narrow shear bands. The introduction of particulates into the glass interferes with the propagating shear band, cause it to slow (or stop) and deflect, thus delaying failure and improving the toughness of the material.

In this paper it will be shown that particulate composites combining a $\text{Zr}_{57}\text{Nb}_5\text{Al}_{10}\text{Cu}_{15.4}\text{Ni}_{12.6}$ matrix with Ta, Nb and Mo particle reinforcements can be successfully processed and that the glass forming ability of the matrix is not significantly affected. Results on the microstructure and mechanical properties will be presented and discussed.

2. Experimental method

In this study, $\text{Zr}_{57}\text{Nb}_5\text{Al}_{10}\text{Cu}_{15.4}\text{Ni}_{12.6}$ alloy (Vit106) [10] was used as a matrix material for composites. Ingots of the matrix alloy were pre-

pared by arc melting a mixture of the elements having a purity of 99.7% or greater. Ingots contained 250 atomic ppm oxygen. Molybdenum, niobium, and tantalum particles were used as reinforcements.

For the composites with a low volume fraction of reinforcements (5–10%) of fine particles, the particles were dispersed in the molten matrix alloy by remelting the alloy in a water cooled copper boat under a Ti-gettered argon atmosphere. The composite ingots were then placed in a quartz tube furnace and vacuum induction remelted at temperatures between 850 and 1100°C, and then injected into a copper mold using high purity argon at 101 kPa pressure. This processing technique is limited to low volume fractions because the increased viscosity of high particulate volume fractions lowers the injection speed too much to achieve the high cooling rate to needed to avoid matrix crystallization.

To fabricate composites of larger particles (30–200 μm) with 50% V_f or greater, particles were placed in the sealed end of a 7 mm I.D. 304 stainless steel tube, the tube was necked about 2 cm above the reinforcement, and ingots of the matrix material were placed into the tube above the neck [13]. The constriction prevents premature matrix/reinforcement contact, minimizing reaction between the melt and the reinforcement. The tube was evacuated and flushed with argon gas several

Table 1

Physical properties of $\text{Zr}_{57}\text{Nb}_5\text{Al}_{10}\text{Cu}_{15.4}\text{Ni}_{12.6}$, molybdenum, niobium and tantalum

Property	$\text{Zr}_{57}\text{Nb}_5\text{Al}_{10}\text{Cu}_{15.4}\text{Ni}_{12.6}$	Mo	Nb	Ta
CTE $10^{-6} \mu\text{m}\times\text{m}^{-1}\times\text{C}^{-1}$	8.7	4.9	7.4	6.6
Elastic modulus (GPa)	86.7	330	103	186
Poisson's ratio, ν	0.38	0.375	0.38	0.35
Density ($\text{g}\times\text{cm}^3$)	6.8	10.22	8.6	16.65
Bulk modulus (GPa)	118	272	143	206
Shear modulus (GPa)	30.8	120	37.5	69
Ultimate strength (MPa)	1800 ^a 1200 ^b	324 (tension)	300	450
Yield strength (MPa)	1800 ^a 1200 ^b	400 (comp.)	207	
Elongation %	2		30	

^a Uniaxial compression.

^b Uniaxial tension.

times to purge residual oxygen prior to heating. The sample tube was left under vacuum on the last cycle to minimize trapped gas, then heated in a resistive tube furnace with temperature feedback control to 975°C, well above the liquidus temperature (820°C) of the glass-forming alloy. The superheat dissolves residual oxides and other impurities that degrade glass-forming ability of the alloy [10]. The sample was held at this temperature for 10 min, then the temperature was lowered to 875°C. When the furnace reached this target temperature, the tube was pressurized with argon to 550 kPa and held for 15 min to allow infiltration of the molten matrix material into the reinforcement. The sample was then quickly removed from the furnace and quenched in the water.

Slices of the composite ingot were examined by X-ray diffraction. The edge of each slice was ground to remove the reaction layer that formed between the metallic glass and the steel tube. The glass transition and crystallization of all samples was studied with a differential scanning calorimeter (Perkin–Elmer DSC 7). The particle/matrix interface in selected samples was examined by electron microprobe and scanning electron microscopy (SEM).

Tensile and compression tests were performed on a universal testing machine (Instron 4200), at constant strain rates between $8 \times 10^{-5} \text{ s}^{-1}$ and $4 \times 10^{-4} \text{ s}^{-1}$. Strain was measured using strain gages attached to the sample surface. The compression samples were 3 mm diameter cylindrical rods with an aspect ratio of 2. The end of each rod was ground flat and perpendicular to the loading axis. Two or three specimens of each composite were tested. Tensile test specimens were machined into dog-bone geometry with a 3 mm diameter gage section and threaded on both ends, in accordance with ASTM standards [14,15]. SEM was used to examine the fracture surfaces.

Composite stresses and physical properties were modeled using both the Eshelby inclusion method and a simple bubble model [16,17,18].

3. Results

Samples of the composites were characterized by X-ray diffraction (Fig. 1). The boxed anno-

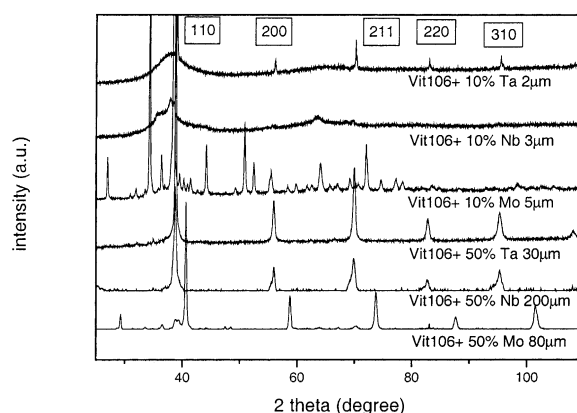


Fig. 1. X-ray diffraction patterns of composites reinforced with Ta, Nb, or Mo particles. Top three patterns show the results for the composites with low volume fraction of small particles and bottom three show the patterns of the composites with high volume fraction of larger particles.

tations denote the reflections from the reinforcement material. The diffraction patterns of the tantalum and niobium reinforced composites show that their matrix is mostly amorphous, but the occurrence of some smaller diffraction peaks, which do not correspond to the pattern of the pure reinforcement, indicate that a new crystalline phase occurs either due to partial crystallization of the matrix or interfacial reactions. The diffraction pattern of the composite with 10% V_f of 5 μm molybdenum particles shows that the sample is fully crystallized, while in composites with 50% V_f of 80 μm molybdenum particles the matrix is only partially crystallized. Calculation shows that a 1 cm^3 , 50% V_f composite of 80 μm spherical particles has 375 cm^2 surface area, while a composite of only 10% V_f of 5 μm particles contains 1200 cm^2 of surface. The number of sites for heterogeneous nucleation to occur increases with surface area. This indicates that the sample can crystallize even with very low volume fractions of reinforcement depending on particle size (particle surface area), the reactivity of the reinforcement and the processing technique (e.g. maximum processing temperature).

Differential scanning calorimetry (DSC) was used to investigate the glass transition and the crystallization behavior of $\text{Zr}_{57}\text{Nb}_5\text{Al}_{10}\text{Cu}_{15.4}\text{Ni}_{12.6}$ metallic-glass (Vit106) and Ta, Mo and Nb metallic-

glass composites. Fig. 2 shows DSC scans of the pure amorphous $\text{Zr}_{57}\text{Nb}_5\text{Al}_{10}\text{Cu}_{15.4}\text{Ni}_{12.6}$ and Ta or Nb reinforced composites using a heating rate of 0.33 K s^{-1} . All samples exhibit an endothermic heat event characteristic of the glass transition followed by two exothermic heat releases indicating the transformation from the metastable undercooled liquid state into crystalline compounds. The temperatures that mark the onset of the glass transition and the first crystallization event are defined as T_g , and T_{x1} , respectively. The T_x ($T_{x1}-T_g$) denotes the supercooled liquid region temperature range. Based on the DSC scans in Fig. 2, it is observed that the addition of Ta or Nb particles into the $\text{Zr}_{57}\text{Nb}_5\text{Al}_{10}\text{Cu}_{15.4}\text{Ni}_{12.6}$ produces no discernible change in either T_g or T_{x1} . Similar results are observed on Mo reinforced composites. In no case did the introduction of the particles negatively affect the thermal stability of the amorphous matrix.

Cross sections of the composite samples were analyzed by scanning electron microscopy (SEM). Microstructures of the composites with 50% V_f are illustrated in Fig. 3. Fig. 3(a) shows the composite reinforced with 30 μm Ta particles. Crystals $\sim 1\text{--}3 \mu\text{m}$ in diameter can be seen in the matrix adjacent to the Ta particles (inset). The compositions of these crystals as measured by microprobe analysis are close to the average matrix composition with an additional 6 atomic% (at.%) Ta. Fig. 3(b) is the

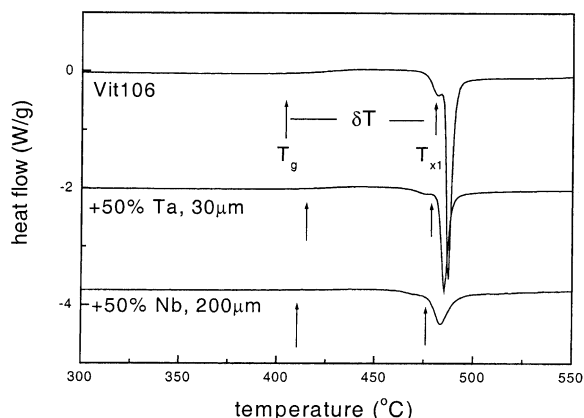


Fig. 2. DSC thermogram (heating rate of 0.33 K s^{-1}) of the $\text{Zr}_{57}\text{Nb}_5\text{Al}_{10}\text{Cu}_{15}$ metallic glass (Vit106) and the Ta or Nb reinforced composites

SEM image of a 200 μm Nb particle reinforced composite; the inset shows the particle/matrix interface. Crystals $\sim 5 \mu\text{m}$ in diameter have formed along the interface. The composition of the crystals is 86 at.% Nb and 12 at.% Zr, with a very small amount of other matrix components. Dark faceted crystals are visible at the matrix. These crystals are similar to the matrix in composition, but with a 50% increase in the Al signal. Fig. 3(c) shows the SEM image of the Mo composite with 80 μm particles. In the inset, one can see crystals ($\sim 3 \mu\text{m}$) appear along, but not directly at, the interface. The compositions of these crystals is 30 at.% Mo and 42 at.% Zr with 5 to 10 at.% of other matrix components. Crystals seem to form preferentially at the interface of the particles in all three composites.

Fig. 4 shows compressive stress-strain curves for unreinforced $\text{Zr}_{57}\text{Nb}_5\text{Al}_{10}\text{Cu}_{15.4}\text{Ni}_{12.6}$ and the particle reinforced composites. Composites containing small particles ($\sim 2\text{--}3 \mu\text{m}$) and low volume fractions of Ta or Nb do not have enhanced strain to failure, and the reinforcement has only a minor effect on the yield stress and ultimate strength of the material. By comparison, composites made with low volume fractions (10% V_f) of larger (150 μm) tungsten and/or tungsten carbide particles or continuous fibers show substantial strain to failure [6,7].

Fig. 5 is a graph of the residual stress distribution in the particle/matrix system, calculated using a simple bubble model [18]. The bubble model is for an isolated particle, but it is reasonably accurate for a dilute system and it is characteristic of residual stress behavior in a non-dilute system. Table 2 lists the peak residual particle hydrostatic stress and matrix hoop and radial stresses calculated for the 50% V_f systems investigated. Because the coefficient of thermal expansion, α_p , is smaller than that of the matrix, α_m , the matrix surrounding the particle is placed in tension when the system cools. The total undercooling, ΔT , used for calculations was 400°C . The stresses diminish by three orders of magnitude within a distance of 3 particle diameters. Cracks or shear bands are guided toward the particles as a result of this tensile hoop stress. Particles with a mean size that is approximately the width of the shear band have

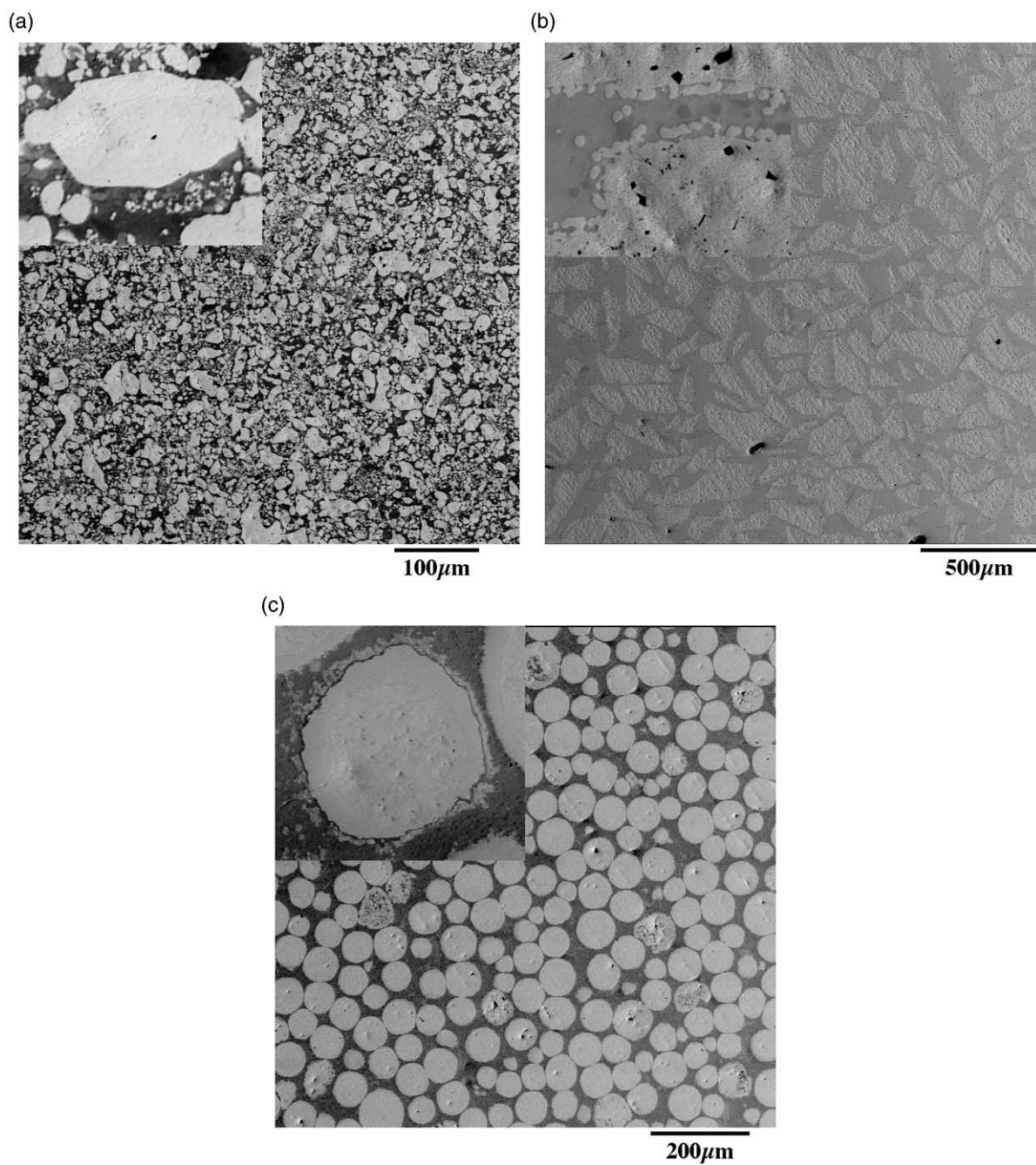


Fig. 3. SEM backscattering image of (a) Ta composite. (b) Nb composite and (c) Mo composite. Inset images are the area around the particle at higher magnification.

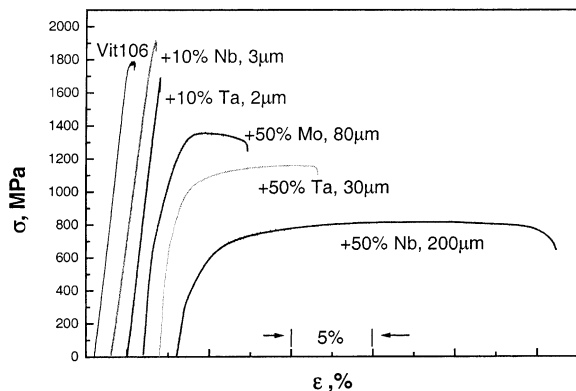


Fig. 4. Compressive stress-strain curves of unreinforced $\text{Zr}_{57}\text{Nb}_5\text{Al}_{10}\text{Cu}_{15.4}\text{Ni}_{12.6}$ and composites. All measurements are displaced by a strain of 1% for better comparison.

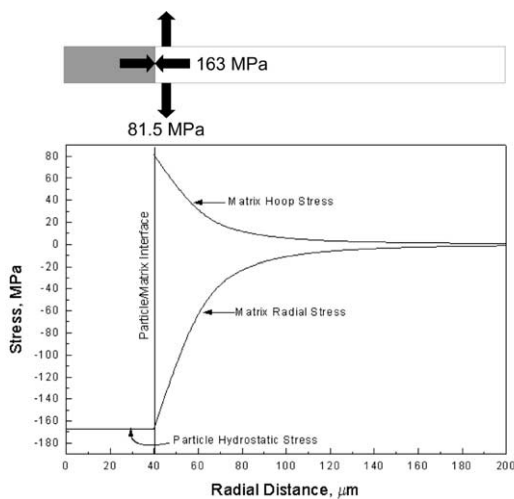


Fig. 5. Graph of hydrostatic, hoop and radial stress distribution calculated for a 50% V_f Mo composite (80 μm particles) using a bubble model.

Table 2

Particle/matrix stress distributions calculated using the bubble model

	Radial stress σ_{rr} , MPa	Hoop stress $\sigma_{\theta\theta}$, MPa	Hydrostatic stress MPa
Niobium	-49.8	24.9	-49.8
Tantalum	-86.3	43.1	-86.3
Molybdenum	-162.7	81.4	-162.7

little effect in stopping its propagation, while larger particles do, independent of particle volume fraction.

Increasing the particle volume fraction to 50% and using larger ($\sim 30\text{--}200\ \mu\text{m}$) particles of Mo, Ta and Nb changes the plastic behavior of the composites dramatically. The yield point of the composite materials is reduced significantly and the strains to failure are increased to values between 6 and 24%. The stress-strain curves show a strong work hardening behavior.

Mean residual stress for each system was also calculated using the Eshelby equivalent inclusion method [16,17]. This model can accommodate both applied stress and thermal strains, and calculations were performed for an unloaded system and at applied stresses in 100 MPa increments. The models only apply within the elastic loading range. The mean residual stresses were then used to calculate the vonMises stresses in the particle and matrix. For the Nb system, the vonMises stress reaches the particle yield at approximately 200 MPa applied stress, approximately the composite yield point shown on the stress-strain diagram. When the particle yields, the matrix must carry a larger portion of the load. The matrix quickly reaches its elastic limit, triggering shear band generation. Residual stresses guide the shear bands toward the reinforcement. The particle plastically deforms, interfering with the nucleation and propagation of shear bands in the amorphous matrix. The model assumes spherical particles; the amount of plastic strain achieved prior to failure depends on the particle shape and the mechanical strength of the particle/matrix interface. The interface strength is dependent upon the processing conditions, which were not varied systematically in this study.

Fig. 6 is an SEM micrograph of the Nb reinforced composite. As seen in Fig. 4, composite reinforced with Nb particles had $\sim 24\%$ plastic strain. While the monolithic metallic-glass fails due to the formation of one catastrophic shear band, the huge plastic strain in the composite is the result of multiple shear band formation. Multiple shear bands form because the particles prevent the propagation of any single shear band.

Fig. 7 is an SEM micrograph of the compressive fracture surface of composite rod reinforced with

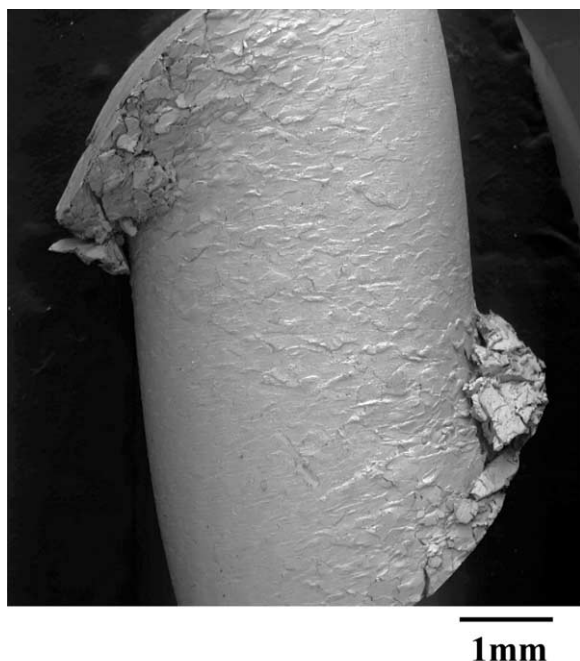


Fig. 6. SEM micrograph of the side of a 50% V_f Nb particles ($\sim 200 \mu\text{m}$) reinforced composite for $Zr_{57}Nb_5Al_{10}Cu_{15.4}Ni_{12.6}$ after compression test showing the formation of multiple shear banding.

Mo particles; the inset image shows a higher magnification of the area close to the particle/matrix interface. The Mo composite sustains about 5% plastic strain, relatively small compared to the Nb or Ta composites. This low ductility is due to the crystals that form along the matrix, making the interface weak and brittle. The inset in Fig. 7 shows a gap at the interface; this gap may be due to a weak interfacial bond, porosity or mechanical tearing during the shear event. This indicates that the load could not be transferred efficiently between the Mo particles and the matrix, resulting in relatively poor mechanical properties.

The Mo and Ta composite tensile samples partially crystallized during processing and fractured prematurely; only the results of unreinforced $Zr_{57}Nb_5Al_{10}Cu_{15.4}Ni_{12.6}$ and the 50% V_f Nb composite (200 μm particles) are discussed. Fig. 8 shows the tensile stress-strain curves for these two materials, along with an Nb composite compression test for comparison. The initial yield point of the composite ($\sim 230 \text{ MPa}$) is more pronounced

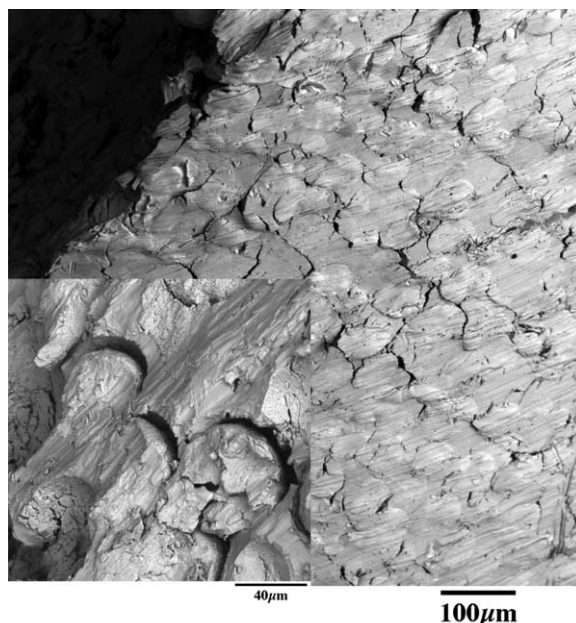


Fig. 7. Compressive fracture surface of 50% V_f Mo composite ($\sim 80 \mu\text{m}$ particles). Inset shows the gap at the particle/matrix interface, indicating poor load transfer between the matrix and reinforcement.

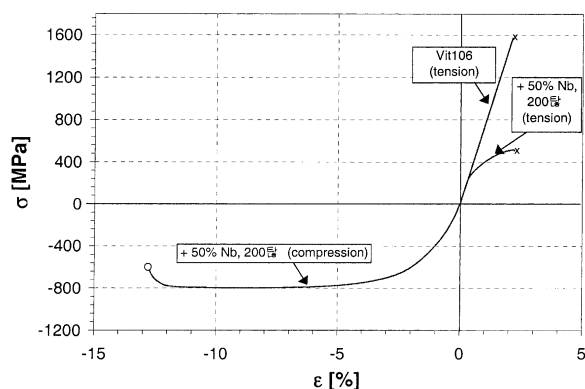


Fig. 8. Compressive and tensile stress-strain curves for the 50% V_f Nb (200 μm) composite and pure $Zr_{57}Nb_5Al_{10}Cu_{15.4}Ni_{12.6}$. x: fracture, o: experiment stopped without fracture.

in tension than in compression, though the yield values are approximately the same. The experimental elastic modulus in the compression sample is 61.3 GPa, 20% lower than the modulus measured under tension (77.5 GPa). The shallower slope of the compression curve serves to mask the initial

yield point. The calculated vonMises stress on the particle at a 200 MPa load is 209 MPa, in good agreement with the published yield for Nb, and this value is the same regardless of loading direction. The average particle and matrix stress with no load is ± 24.7 MPa (fiber in compression, matrix in tension) and the principle value when the sample is under load is roughly equal to the load \pm the initial residual stress. The strain-to-failure and ultimate strength of the composite is much greater in compression than tension; the tensile stress-strain curve shows work hardening from the beginning of plasticity at 0.4% strain up to the failure strain of 2.21%. The tensile strength for the Nb composite measured on the two samples was 510 and 517 MPa. The tensile samples fail in the same way as the compression samples, up to a point. After the particles yield the load is primarily carried by the matrix, and the applied stress rapidly approaches the matrix ultimate tensile strength of 1200 MPa, triggering shear band initiation and propagation. Under compressive loading the composite is constrained, cracks cannot open and the distance a shear band can propagate is limited, encouraging the formation of multiple shear bands. However, under tensile loading cracks in the material are not constrained, the shear bands become unstable and fracture occurs. Also, the particle/matrix interface plays a smaller role when the sample is under compression, because a tight bond is not needed to transfer load or adhere the matrix to the reinforcement as it is when loaded in tension. As a result, the total plastic strain in tension is significantly less than in compression and almost identical to the failure strain of the pure matrix material (failure at $\sigma=1570$ MPa, $\epsilon=2.13\%$, also shown in Fig. 4).

Elastic moduli calculated using the Eshelby equivalent inclusion method versus measured elastic moduli are listed in Table 3, for a fiber volume fraction of 50%. Agreement between the values is quite good, the closest agreement is found with Ta (7.5%) and the largest disparity with Nb (17%). The variation reflects the strength of the interfacial bond, the effect of porosity in the sample, and the accuracy of the experimental measurements.

Table 3

Calculated and measured elastic moduli for Nb, Ta and Mo reinforced $\text{Zr}_{57}\text{Nb}_5\text{Al}_{10}\text{Cu}_{15.4}\text{Ni}_{12.6}$ metallic-glass matrix composites

Reinforcement, $V_f=0.5$	Measured elastic modulus, GPa	Calculated elastic modulus, GPa
Niobium	94.5	77.5
Tantalum	126	116.5
Molybdenum	160	137.5

4. Conclusion

$\text{Zr}_{57}\text{Nb}_5\text{Al}_{10}\text{Cu}_{15.4}\text{Ni}_{12.6}$ bulk metallic glass forming liquids were reinforced with Mo, Nb, and Ta particles. The composites were characterized with respect to their structure, microstructure and thermal properties. The thermal stability of the matrix did not deteriorate after adding the particles. For all three composites, crystals have been formed near the interface between the particle and the matrix. Adding low volume fraction of small particles of Ta or Nb does not enhance strains to failure and has only a minor effect on the yield stress and ultimate strength of the material. Adding high volume fraction of larger particles of Mo, Ta and Nb changes the plastic behavior of the composites dramatically. The yield point of the composite is reduced significantly and the compressive strain to failure is increased by a factor of up to 12, to values between 6 and $\sim 24\%$. The amount of plastic strain achieved prior to failure depends upon several factors: the residual stress arising from the mismatch in thermal expansion and particle shape, and the mechanical strength of the particle/matrix interface (and thus on the processing conditions). The amount of total plastic strain in tension is significantly less than in compression and almost identical to the failure strain of the pure matrix material $\text{Zr}_{57}\text{Nb}_5\text{Al}_{10}\text{Cu}_{15.4}\text{Ni}_{12.6}$.

Acknowledgements

This work was supported by US Army Research Office under grant number DAAD19-01-1-0525.

References

- [1] Strife JR, Prewo KM. *J. Mater. Sci* 1982;7:359.
- [2] Vaidya RU, Norris C, Subramanian KN. *J. Mater. Sci.* 1992;27:4957.
- [3] Vaidya RU, Chawla KK, Subramanian KN. *J. Mater. Sci.* 1984;29:1719.
- [4] Kimura H, Cunningham B, Ast DG. In: Masumoto T, Suzuki K, editors. *Proc. 4th Int. Conf. On Rapidly Quenched Metals*. Sendai: Japan Instit. Metal; 1982.
- [5] Zielinski PG, Ast DG. In: Kear BH, Giessen BC, editors. *MRS Symposia Proc. Rapidly Solidified Metastable Materials*. New York: Elsevier; 1984. p. 18-9.
- [6] Conner RD, Dandliker RB, Johnson WL. *Acta metal* 1998;46:6089.
- [7] Conner RD, Choi-Yim H, Johnson WL. *J. Mater. Res.* 1999;14:3292.
- [8] Peker A, Johnson WL. *Appl. Phys. Lett* 1993;63:2342.
- [9] Lin X, Johnson WL. *J of Appl. Phys* 1995;78:6514.
- [10] Lin X, Lin X, Johnson WL. *Mater. Trans. JIM* 1997;38:473 Ph.D. thesis.
- [11] Choi-Yim H, Johnson WL. *Appl. Phys. Lett* 1997;71:3808.
- [12] Choi-Yim H, Busch R, Koester U, Johnson WL. *Acta metall* 1999;47:2455.
- [13] Dandliker RB, Conner RD, Johnson WL. *J. Mater. Res.* 1998;13:2896.
- [14] ASTM E8-90a. *Tension Testing of Metallic Materials*, Annual Book of ASTM Standards, 1990.
- [15] ASTM E9-89a. *Compression Testing of Metallic Materials at Room Temperature*, Annual Book of ASTM Standards, 1989.
- [16] Eshelby JD. *Proc. R. Soc., London* 1957;A241:376.
- [17] Eshelby JD. In: Sneddon IN, Hill R, editors. *Progress in Solid Mechanics*. Amsterdam: North Holland Publishing Co; 1961. p. 8-9.
- [18] Clyne TW, Withers PJ. In: Davis EA, Ward IM, editors. *An Introduction to Metal Matrix Composites*. Cambridge University Press; 1993.